Prism Computational Sciences, Inc.
455 Science Drive, Suite 140
Madison, WI 53711

Modeling of Inner-Shell (Kα, Kβ) Line Emission from Cu Targets Heated by Short Pulse Lasers

J. J. MacFarlane, I. E. Golovkin, P. R. Woodruff

Prism Computational Sciences, Inc.

PCS-R-113

August 2010

Table of Contents

1. Introduction

This report describes the modeling of inner-shell line emission from Cu targets irradiated by short pulse lasers. In short-pulse laser experiments, energetic (or "hot") electrons are generated through the interaction of high intensity laser light with the target material. As the hot electrons propagate through the target, they collide with target ions, and have energies sufficient to eject *1s* (K-shell) electrons from the target ions. These K-shell vacancies are then quickly filled by electrons from outer shells. Thus, even though a target may be relatively cold and have many bound electrons, it still produces x-ray emission as a result of the hot electrons. Kα emission results from $2p \rightarrow 1s$ transitions, while Kβ emission results from $3p \rightarrow 1s$ transitions. Measurements of the x-ray spectral emission provide information on the characteristics of both the target material (*e.g.*, ionization state, and from that, the "thermal" temperature), and the hot electrons (*e.g.*, amount of hot electrons, as more hot electrons produce higher K-shell emission fluxes).

Experiments have recently been performed at the University of Rochester's Laboratory for Laser Energetics (LLE) in which time-resolved Kα spectra from Cu targets were recorded for targets of different sizes. The spectra clearly show different levels of heating by the hot electrons, as the smaller targets exhibit spectra from Cu at significantly higher degrees of ionization. In this memo, we describe modeling used in PrismSPECT and SPECT3D that can be used in analyzing spectral data (and, in the case of SPECT3D, images and absolute flux levels) obtained in these experiments.

2. Modeling of Kα/Kβ Emission

Prism's spectral analysis codes (PrismSPECT and SPECT3D) can be used to compute Kα and Kβ spectra, images, and flux levels for materials which have hot electron components to their electron distributions. Consider the following transitions for target ions originally with 8 and 9 bound electrons (*e.g.*, Cu XXII and Cu XXI):

$$1s^2 2s^2 2p^4 \xrightarrow{e^- \text{ impact}} 1s^1 2s^2 2p^4 \xrightarrow{K\alpha \text{ emission}} 1s^2 2s^2 2p^3 \quad (1)$$

$$1s^2 2s^2 2p^4 3p^1 \xrightarrow{e^- \text{ impact}} 1s^1 2s^2 2p^4 3p^1 \xrightarrow{K\alpha \text{ emission}} 1s^2 2s^2 2p^3 3p^1 \quad (2)$$

$$1s^2 2s^2 2p^5 \xrightarrow{e^- \text{ impact}} 1s^1 2s^2 2p^5 \xrightarrow{K\alpha \text{ emission}} 1s^2 2s^2 2p^4 \quad (3)$$

$$1s^2 2s^2 2p^4 3p^1 \xrightarrow{e^- \text{ impact}} 1s^1 2s^2 2p^4 3p^1 \xrightarrow{K\beta \text{ emission}} 1s^2 2s^2 2p^4 \quad (4)$$

In each case, an energetic electron ejects a *1s* electron from the target ion via electron-impact ionization. In the first three cases, the *1s* vacancy is filled by a *2p* electron ($2p \rightarrow 1s \Rightarrow$ Kα emission), while in the last case the *1s* vacancy is filled by a *3p* electron ($3p \rightarrow 1s \Rightarrow$ Kβ emission). The Kβ emission is at a significantly higher energy (shorter wavelength) than the Kα emission. For the first two cases, the wavelengths of the Kα emission are nearly the same;

the wavelength in the third case is more highly shifted. This occurs because screening effects are dominated by the number of electrons in the L-shell. The "spectator" electron in the *3p* subshell (Eq. (2)) produces only a very modest shift in wavelength.

Note that the shift in the observed wavelength of the emission in experiments is due to the change in the state of the plasma. That is, as the ionization distribution and the populations of various excited states change, the Kα and Kβ emission originates from different ions and atomic levels. As the target plasma heats up, higher ionization and excitation states are populated, and these ions tend to produce Kα and Kβ emission at slightly shorter wavelengths. Thus, recording time-resolved spectra provides a measure of the time-dependent ionization in the target plasma.

Next, consider the Kα and Kβ emission from lower ionization stages of Cu, with 16 and 17 bound electrons (Cu XIV and Cu XIII):

$$1s^2 2s^2 2p^6 3s^2 3p^4 \xrightarrow{e^- \text{ impact}} 1s^1 2s^2 2p^6 3s^2 3p^4 \xrightarrow{K\alpha \text{ emission}} 1s^2 2s^2 2p^5 3s^2 3p^4 \quad (5)$$

$$1s^2 2s^2 2p^6 3s^2 3p^5 \xrightarrow{e^- \text{ impact}} 1s^1 2s^2 2p^6 3s^2 3p^5 \xrightarrow{K\alpha \text{ emission}} 1s^2 2s^2 2p^5 3s^2 3p^5 \quad (6)$$

$$1s^2 2s^2 2p^6 3s^2 3p^4 3d^1 \xrightarrow{e^- \text{ impact}} 1s^1 2s^2 2p^6 3s^2 3p^4 3d^1 \xrightarrow{K\alpha \text{ emission}} 1s^2 2s^2 2p^5 3s^2 3p^4 3d^1 \quad (7)$$

$$1s^2 2s^2 2p^6 3s^2 3p^5 \xrightarrow{e^- \text{ impact}} 1s^1 2s^2 2p^6 3s^2 3p^5 \xrightarrow{K\beta \text{ emission}} 1s^2 2s^2 2p^6 3s^2 3p^4 \quad (8)$$

Again, the number of Kα and Kβ photons emitted is proportional to the number of K-shell vacancies produced by electron-impact ionization, which is in turn proportional to the number of hot electrons. As in the L-shell ion examples (Eqs. 1-4), the first 3 transition sequences (Eqs. 5-7) result in Kα line emission, while the last results in Kβ emission.

But there are some important differences between these transitions and those listed in Eqs. (1-4). First, the Kα emission from these M-shell ions (Eqs. 5-8) tends not to be susceptible to opacity effects (*i.e.*, resonant self-absorption) as the L-shell cases (Eqs. 1-4). This is because for the bulk of the plasma, essentially all of the ions in the target plasma will have filled *2p* subshells. For the Kα emission in Eqs. (5-7) to be re-absorbed via a *1s→2p* transition, an ion must be in a state having an electronic configuration with a partially open *2p* subshell, and only an extremely small number of ions will be in such a state at temperatures where these ions are prevalent. On the other hand, a high fraction of these ions will have states with partially open *3p* subshells. Thus, for ions of the type shown in Eqs. (5) to (8), the Kα emission is optically thin while the Kβ emission is readily re-absorbed.

Second, because there are a large number of bound electrons for these lower ionization stages, the atomic modeling becomes more complex because the number of atomic energy levels and transitions to be considered increases significantly. Because of this, we have chosen to model the Kα and Kβ production in PrismSPECT and SPECT3D differently for L-shell ions and M-shell ions (*i.e.*, roughly speaking, ions with 10 or less bound electrons versus 11 or more bound electrons). Below, we discuss the modeling for these two classes of ions.

Copper Atomic Physics Database

The atomic physics database for Cu includes energy level and transition data for all ions. Atomic cross section data are generated using the ATBASE suite of codes [1]. This suite of codes is composed of a collection of publicly available codes [2-5] and a series of codes developed and refined by Wang *et al.* [6,7]. Energy level data include energies, statistical weights, *j* values, and mean square orbital radii. Transition data include electron-impact ionization and excitation cross sections and rate coefficients, oscillator strengths, photoionization cross sections and radiative recombination rate coefficients, autoionization rates and dielectronic recombination rate coefficients, and proton-impact ionization and excitation cross sections. Additional details regarding the atomic database for Cu are discussed below.

2.1 Modeling for L-Shell Ions

Energy Levels, Transition Energies, and Atomic Data

Energy levels for a large number of autoionizing states with a single K-shell vacancy are included in the atomic physics database for L-shell ions. For Cu, the total number of (fine structure) energy levels included in the database for Li-like to Ne-like Cu is 11,300. Of this, approximately 20 – 25% are autoionization states with *1s* vacancies (*e.g.*, $1s^1 2s^2 2p^4 3p^1$ and $1s^1 2s^2 2p^5$). The energy of each of the levels is computed using a Hartree-Fock atomic structure model [2,6]. The transition energies (wavelengths) are simply the differences in energy between two atomic levels.

For L-shell ions, $1s^1$ autoionization states (*i.e.*, levels having a single electron in the K-shell) are included explicitly in the atomic model. Collisional coupling between states is complete – *i.e.*, all thermal (non-autoionizing) and autoionizing states are collisionally coupled – with electron-impact collisional excitation and ionization cross sections computed using a distorted wave (DW) model [8]. The DW calculations include exchange effects, and therefore provide reliable cross sections for both spin-conserved ($\Delta S = 0$) and spin change ($\Delta S > 0$) transitions.

Dielectronic recombination processes involving autoionization states of Ne-like ions and higher are treated explicitly, with electron capture rates determined from detailed balance with their corresponding autoionization rates. For lower ionization stages (M-, N-, O-shell, etc.), autoionization states are not explicitly included in the atomic model, and effective dielectronic recombination rates are utilized.

Rate Equations

In PrismSPECT and SPECT3D, if designated to be in LTE, the populations are computed using the Saha equation and Boltzmann statistics [9]. For non-LTE calculations, populations are determined from the solution of a coupled set of atomic rate equations. The rate equation for atomic level *i* can be written as:

$$\frac{dn_i}{dt} = -n_i \sum_{i \neq j}^{N_L} W_{ij} \quad + \quad \sum_{i \neq j}^{N_L} n_j \, W_{ji} \quad , \tag{9}$$

where W_{ij} and W_{ji} represent the depopulating and populating rates between levels i and j, n_i and n_j are the number densities of levels i and j, and N_L is the total number of levels in the system. For upward transitions ($i < j$),

$$W_{ij} = \begin{cases} n_e \, C_{ij} + B_{ij} \overline{J_{ij}} & \text{(excitations)} \\ \\ n_e \, \gamma_{ij} + \beta_{ij} + \Omega_{ij} & \text{(ionizations)} \end{cases} \tag{10}$$

while for downward transitions ($i > j$),

$$W_{ji} = \begin{cases} n_e \, D_{ji} + A_{ji} + B_{ji} \overline{J_{ij}} & \text{(deexcitations)} \\ \\ n_e^2 \, \delta_{ji} + n_e (\alpha_{ji}^{RR} + \alpha_{ji}^{DR}) & \text{(recombinations)} \end{cases} \tag{11}$$

where n_e is the electron density; $\overline{J_{ij}}$ is the frequency-averaged mean intensity of the radiation field over a line profile; C_{ij}, γ_{ij}, D_{ji}, and δ_{ji} are rate coefficients for collisional excitation, ionization, deexcitation, and recombination; A_{ji}, B_{ij}, and B_{ji} are Einstein coefficients for spontaneous emission, and stimulated absorption and emission; β_{ij} is the photoionization rate; Ω_{ij} is the autoionization rate; α_{ji}^{RR} is the radiative recombination rate coefficient; and α_{ji}^{DR} is the dielectronic recombination rate coefficient (or, in the case of treating dielectronic recombination using explicit autoionization levels, the electron capture rate coefficient).

For plasmas with non-Maxwellian electron distributions, collisional excitation and ionization rates are computed by integrating the electron distribution over the electron kinetic energy:

$$n_e \, C_{\ell u} = n_e \int_{E_0}^{\infty} d\varepsilon \; \upsilon_e \, f(\varepsilon) \; \sigma_{\ell u}(\varepsilon) \tag{12}$$

where ε is the electron kinetic energy, υ_e is the electron velocity, $f(\varepsilon)$ is the electron distribution function, $\sigma_{\ell u}(\varepsilon)$ is the electron-impact excitation/ionization cross section, and E_0 is the threshold energy. For collisional deexcitation, the rate is obtained using the microscopic reversibility relation, where:

$$\sigma_{u\ell}(\varepsilon) = \frac{g_\ell}{g_u}\,\frac{\varepsilon+\varepsilon_{\ell u}}{\varepsilon}\,\sigma_{\ell u}(\varepsilon+\varepsilon_{\ell u}) \qquad (13)$$

where g_u and g_ℓ are the statistical weights of the upper (u) and lower (ℓ) levels, and $\varepsilon_{\ell u}$ is the transition energy. For collisional recombination, we approximate the rate coefficient for the case of a non-Maxwellian electron distribution by using the detailed balance relationship in conjunction with a "mean electron temperature" for the electron distribution.

2.2. Modeling for M-Shell Ions

For ions with more than 10 bound electrons, PrismSPECT and SPECT3D model $1s^1$ autoionization states differently than the L-shell case. This is motivated by the fact that atomic structure of ions becomes significantly more complex (*i.e.*, the number of atomic energy levels and transitions is significantly larger) as the number of bound electrons increases.

A total of approximately 20,000 atomic levels is included in the atomic physics database for ions ranging from Cu I to Cu XIX (Na-like Cu). For these ions, level bundling is often used (*i.e.*, fine structure levels are bundled together).

Energy Levels, Transition Energies, and Atomic Data

For *non-autoionizing* states, atomic level populations are computed using the same approach as described above in Section 2.1. For $1s^1$ autoionization states, the populations and resulting Kα/Kβ emission are computed differently. In this case, a configuration averaged model is used for autoionization states (*i.e.*, no L-S term split or fine structure splitting of levels). The populations are computed using the following assumptions:

- the sum of the populations of the autoionization states is small (*i.e.*, much less than the "thermal" non-autoionizing states);
- the primary populating mechanisms for the autoionization states are electron-impact ionization and electron-impact excitation of a *1s* electron;
- the primary depopulating mechanisms for the autoionization states are either a spontaneous emission that results in the re-filling of the *1s* subshell (Kα, Kβ, Kγ, …) or an autoionization (a radiationless transition where one or more additional electrons is ejected).

These assumptions should be valid for typical conditions in short-pulse laser experiments. One of the ramifications of the second and third assumptions is that the coupling between autoionization states is weak (*i.e.*, one autoionization state is not being either populated or depopulated through transitions between it and another autoionization state). However, if this were to occur, the Kα/Kβ spectrum would not change significantly unless the Kα/Kβ wavelengths for the two autoionizing levels were noticeably different.

Unlike the L-shell case, the *1s* autoionizing levels and transition rates are not extracted from the database, but instead are set up during a PrismSPECT or SPECT3D run. For each of the non-autoionizing electron configurations (*i.e.*, "thermal" levels) in a given calculation, a corresponding autoionizing level with a *1s* vacancy is added to the atomic model, along with

levels with *1s* vacancies that can be produced by excitation. Kα and Kβ transition energies are given by:

$$\Delta E_{ul} = \Delta E_0 + \Delta E_{vac} \quad , \tag{14}$$

where ΔE_0 is the cold Kα/Kβ transition energy for Cu I [10], and ΔE_{vac} is an energy shift that depends on the number of vacancies in the $n = 2$ and $n = 3$ shells. The value of the shift is based on the experimental measurements of Tanis *et al.* [11], where for Cu we compute the energy shift (in eV) using:

$$\Delta E_{vac}(K\alpha) = 1.54\,(A-2)\,N_2 + \ 0.15\,(A-2)\,N_3 \quad , \tag{15}$$

and

$$\Delta E_{vac}(K\beta) = 2.97\,(A-2)\,N_2 + \ 0.30\,(A-2)\,N_3 \quad , \tag{16}$$

where A is the atomic number (= 29 for Cu), N_2 is the number of vacancies in the *2s* and *2p* subshells, N_3 is the number of vacancies in the *3s* and *3p* subshells.

When computing the spectra, line widths are taken from the experimental results of Holzer *et al.* [12].

<u>*Rate Equations*</u>

The population of an autoionizing level, u, is computed by solving the rate equation:

$$\frac{dn_u}{dt} \ = \ \sum_l n_l \, C_{lu} - n_u \, (\Gamma_{uL} + \sum_l A_{ul}) \quad , \tag{17}$$

where n_u is the upper (autoionizing) state population density, and C_{lu} is the collisional ionization or excitation from the lower state, l. Γ_{ul} is the autoionization rate, and the A_{ul} are the spontaneous emission rates for Kα, Kβ, Kγ, ... lines. The first summation is over all entrance channels, which includes collisional ionizations (via ejection of a *1s* electron) and collisional excitations (excitation of a *1s* electron).

For M-shell ions, the collisional rates are computed using Eqs. (12) and (13), and semi-empirical cross sections. For collisional excitation, we calculate the cross section using the method described in Ref. [13] (see also [14]):

$$\sigma_{lu}(\varepsilon) \ = \ \frac{8\pi^2 a_o^2}{\sqrt{3}} \left(\frac{I_H}{\Delta E_{lu}} \right)^2 f_{ul} \, \frac{g(U)}{U'} \left(1 - \frac{1}{U'} \right) \quad , \tag{18}$$

where ε is the electron kinetic energy, ΔE_{lu} is the transition energy, $U = \varepsilon / \Delta E_{lu}$, $U' = \min(U, 100)$, f_{ul} is the oscillator strength, I_H is the ionization potential of hydrogen, and $g(U)$ is the Gaunt factor given by Mewe [15]:

$$g(U) \ = \ 0.15 + 0.28 \log(U) \ . \tag{19}$$

Limiting the value of U in computing the cross section (*i.e.*, using U' instead of U in Eq. (18)) is done to account for relativistic effects at high electron kinetic energies.

The collisional ionization cross section is given by [13,16]:

$$\sigma_{lK}(\varepsilon) \;=\; 2\pi a_o^2 \;\xi \left(\frac{I_H}{\Phi_K}\right)^2 \left(\frac{1}{y}\right) \log\left(y\right)\; W\left(y\right) \;, \tag{20}$$

where $y = \varepsilon/\Phi_K$, Φ_K is the ionization potential for the *1s* electron, ξ is the number of electrons in the subshell,

$$W(y) \;=\; \left(\log(y)\right)^{\beta/y} \;, \tag{21}$$

and

$$\beta \;=\; \frac{1}{4}\left(\sqrt{\frac{100q+91}{4q+3}} - 5\right) \;, \tag{22}$$

where q is the ion charge.

The autoionization rate is given by:

$$\Gamma_{uL} = \sum_l A_{ul} \;\left(\frac{1-\omega_K}{\omega_K}\right) \;, \tag{23}$$

where ω_K is the fluorescence yield. For the M-shell ions, the fluorescence yield for is taken from Hubbell *et al.* [17]. Spontaneous emission rate values are taken from Scofield [18].

2.3. Emission Spectra

For a given population distribution, the frequency-dependent opacity and emissivity are determined by summing over the contributions of all bound-bound (*bb*), bound-free (*bf*) and free-free (*ff*) transitions [19]:

$$\begin{aligned} \kappa_\nu \;=\; & \sum_u^{N_L} \sum_{u>\ell} \left[n_\ell - \frac{g_\ell}{g_u} n_u \right] \alpha_{\ell u}^{bb}(\nu) \\ & + \;\; \sum_\ell^{N_L} \sum_{u>\ell} \left[n_\ell - n_\ell^* e^{-h\nu/kT} \right] \alpha_{\ell u}^{bf}(\nu) \;+\; \sum_q^{N_{Ion}} n_e n_{q+1} (1 - e^{-h\nu/kT})\, \alpha^{ff}(\nu) \end{aligned} \tag{24}$$

and

$$\eta_\nu = \left(\frac{2h\nu^3}{c^2}\right)\left\{\sum_u^{N_L}\sum_{u>\ell}\frac{g_\ell}{g_u}\,n_u\,\alpha_{\ell u}^{bb}(\nu) + \sum_\ell^{N_L}\sum_{u>\ell} n_\ell^*\,e^{-h\nu/kT}\,\alpha_{\ell u}^{bf}(\nu) + \sum_q^{N_{Ion}} n_e\,n_{q+1}\,e^{-h\nu/kT}\,\alpha^{ff}(\nu)\right\} \quad (25)$$

where T is the electron temperature, n_i is the number density of atoms in level i, n_ℓ^* is the LTE population of state n_ℓ computed using the actual density of the upper state of the bound-free transition, n_{q+1} is the number density of atoms in ionization stage q+1 summed over all excitation levels, N_L is the total number of atomic levels, h is Planck's constant, k is Boltzmann's constant, and c is the speed of light. The bound-bound cross section is given by:

$$\alpha_{\ell u}^{bb}(\nu) = \left(\frac{\pi e^2}{m_e c}\right) f_{u\ell}\,\phi_{u\ell}(\nu) \quad (26)$$

where $f_{u\ell}$ is the transition oscillator strength, $\phi_{u\ell}(\nu)$ is the line profile, and e and m_e are the electron charge and mass, respectively. The frequency-dependent bound-free cross section, $\alpha_{\ell u}^{bf}(\nu)$, is based on tabulated results from atomic structure calculations. The free-free cross section is given by:

$$\alpha^{ff}(\nu) = \left(\frac{4e^6}{3ch}\right)\left(\frac{2\pi}{3km_e^3}\right)^{1/2}\overline{g_{ff}}\,Z_q^2\,T^{-1/2}\,\nu^{-3} \quad (27)$$

where $\overline{g_{ff}}$ is the free-free Gaunt factor [20], and Z_q is the ion charge.

Line profiles are modeled using a Voigt profile, and include natural (including autoionization), Doppler, and Stark broadening. In general, bound-bound Stark widths are determined using the semi-empirical model of Griem [21]:

$$\Delta\omega_{Stark} = 8\left(\frac{\pi}{3}\right)^{3/2}\frac{\hbar}{ma_0}n_e\left(\frac{E_H}{kT_e}\right)^{1/2}\left[\left\langle r_\ell^2\right\rangle\overline{g_\ell} + \left\langle r_u^2\right\rangle\overline{g_u}\right] \quad (28)$$

where $\left\langle r_i^2\right\rangle$ and $\overline{g_i}$ are the mean square orbital radius and Gaunt factor of state i, E_H is the ionization energy of hydrogen, and a_0 is the Bohr radius. A Gaunt factor of 0.2 is used for all lines.

Continuum lowering effects are modeled using an occupation probability model [22], supplemented by the ionization potential depression formalism of More [23]. The occupation probability model produces a continuous reduction in the effective statistical weights of energy levels with increasing density, so that the relatively high-n states (n = principal quantum number) cannot be populated at high densities. This occupation probability formalism compares favorably with results from ion microfield calculations of argon at high densities [24] using the APEX code [25]. The ionization energy thresholds are depressed using the More model, which results in an enhancement of ionization rates and a shift in the location of bound-free edges in computed spectra.

For SPECT3D, the specific intensity, I_ν^{Det}, at a detector pixel is computed along each line of sight by solving the integral form of the radiative transfer equation [19]:

$$I_\nu^{Det} = I_\nu^{BL} e^{-\tau_{Max}} + \int_0^{\tau_{Max}} S_\nu \; e^{-\tau_\nu} \; d\tau_\nu \tag{29}$$

where

$$S_\nu = \eta_\nu / (\kappa_\nu + \sigma_\nu) \quad , \tag{30}$$

$$\tau_\nu(z) = \int_0^z \kappa_\nu \; dz \quad , \tag{31}$$

η_ν is the plasma emissivity at frequency ν, κ_ν is the absorption coefficient, σ_ν is the scattering coefficient, $\tau_\nu(z)$ is the optical depth as measured to a position z along the line of sight relative to the detector, τ_{Max} is the total optical depth along the line of sight, and I_ν^{BL} is the specific intensity at the back boundary of the plasma (defined by the backlighter intensity). For PrismSPECT, Eq. (29) is solved for a single line-of-sight that runs through its one and only volume element, and is perpendicular to the volume element surface.

In SPECT3D, the total flux at the detector, $\mathcal{F}_\nu$, is given by summing over lines of sight, ℓ:

$$\mathcal{F}_\nu = \sum_\ell^{N_{LOS}} \mathcal{F}_\nu^\ell \tag{32}$$

where

$$\mathcal{F}_\nu^\ell = I_{\nu,\ell}^P \, \Delta\Omega_P^\ell + I_{\nu,\ell}^{BL} \; e^{-\tau_{\max}} \, \Delta\Omega_{BL} \quad , \tag{33}$$

$I_\nu^P = I_{\nu,\ell}^{Det} - I_{\nu,\ell}^{BL} \; e^{-\tau_{Max}}$ is the contribution to the specific intensity at the detector that is due to the self-emission from the plasma, $\Delta\Omega_P^\ell$ is the solid angle of the plasma seen by the detector for line of sight ℓ, and $\Delta\Omega_{BL}$ is the solid angle of the backlighter seen by the detector.

SPECT3D generates time-resolved filtered images by computing the frequency-integrated specific intensity for each detector pixel:

$$I_\ell^{Det} = \int_{\nu_{\min}}^{\nu_{\max}} I_{\nu,\ell}^{Det} \; R_\nu \; d\nu \quad , \tag{34}$$

where $\nu_{\min}$ and $\nu_{\max}$ are the minimum and maximum photon energies, respectively, and R_ν is the frequency-dependent filter response function. Time-resolved spectra are based on the frequency-dependent *flux at the detector*. The 2-D space-integrated spectra (*i.e.,* integrated over the entire detector grid) are computed using Eq. (32). Horizontally and vertically resolved spectra are frequency-dependent spectra that are integrated in one dimension of the detector plane, but spatially resolved in the other dimension. In this case, the frequency-dependent flux at the detector per resolution element is computed.

3. Example Kα/Kβ Emission Spectra for Copper

Here, we present several examples of calculated Kα/Kβ emission for Cu. The first set of results are from PrismSPECT calculations, which is a single volume element code. We note that the same physics modules are used for the SPECT3D and PrismSPECT codes.

Figures 3.1 through 3.3 show the results from steady-state PrismSPECT calculations for a 5 μm-thick, solid-density Cu slab where the temperature was varied from T = 10 eV to 500 eV. The electron distribution included a hot electron component where 0.1% of the electrons were at T_{hot} = 200 keV.

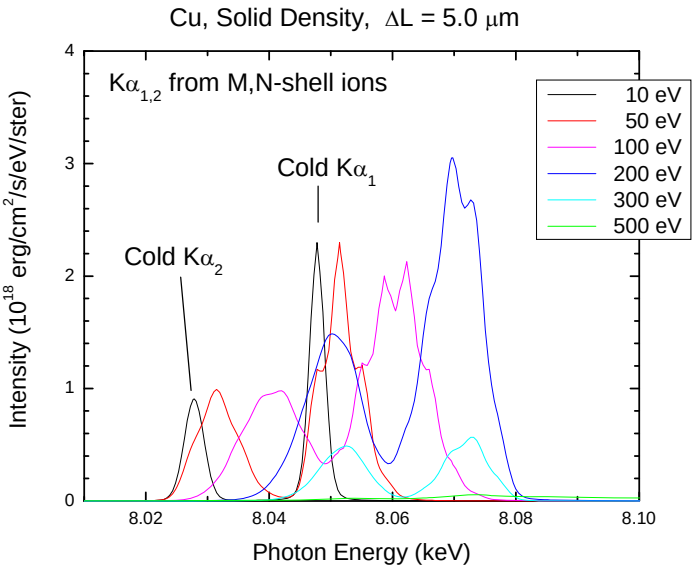

Figure 3.1. Calculated Kα emission spectra for a 5 μm-thick solid-density Cu target. Spectra are shown for temperatures ranging from 10 eV to 500 eV.

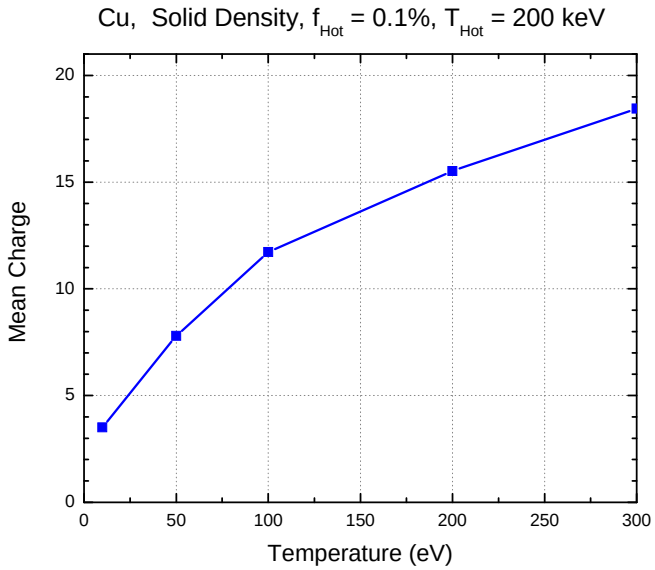

Figure 3.2. Calculated mean charge state for solid-density Cu as a function of temperature.

Figure 3.1 shows the emission spectra, while Fig. 3.2 shows the dependence of the mean ionization of the Cu on temperature. The spectral region shown covers the $h\nu$ = 8.0 – 8.1 keV region, where the cold Kα_1, Kα_2 features are shown in detail. At temperatures $\lesssim$ 300 eV, the emission is dominated by Kα_1, Kα_2 in this spectral regime. At these temperatures, the L-shell remains filled (*i.e.*, there are very few *2p* vacancies), and therefore no Kα resonant self-absorption occurs. At temperatures $\lesssim$ 300 eV, there is a slight shift of the Kα emission to higher photon energies with increasing temperature, as the number of electrons in the M-shell (*3s, 3p, 3d* subshells) decreases. At higher temperatures, *2p* vacancies are created as the plasma becomes more ionized, and the Kα emission shifts more strongly to higher photon energies ($h\nu$ > 8.1 keV).

Figure 3.3 shows the optical depth from the same set of calculations in the $h\nu$ = 8 – 10 keV range. Note that the Kα lines do not become optically thick until temperatures reach > 200 eV, as there is very little optical depth due to resonant self-absorption in the $h\nu$ = 8.0 – 8.1 keV region. The Kβ lines at $h\nu \gtrsim$ 8.9 keV, however,, are optically thick at $T \gtrsim$ 50 eV, as the Cu ions contain a significant number of *3p* vacancies. Fig. 3.3 also shows that the optical depth of the Kα lines shifts from $h\nu$ ~ 8.1 keV to $h\nu$ ~ 8.4 keV as the Cu shifts in ionization through the L-shell (*i.e.*, from Ne-like to Li-like Cu) as the temperature increases from 300 eV to 1 keV. This effect is also seen in the Kβ lines at $h\nu$ ~ 9.3 keV to $h\nu$ ~ 9.8 keV.

To further see the effects of resonant self-absorption on the Kβ lines, Figure 3.4 shows emission spectra from Cu targets with two thicknesses, 0.05 μm and 5 μm. For the 0.05 μm-thick target, there is significant Kα emission at $h\nu$ ~ 8.2 – 8.4 keV at T = 750 eV due to L-shell ions (*i.e.*, relative to the intensity of the $h\nu$ = 8.0 – 8.1 keV emission). However, in the 5 μm-thick Cu case, the L-shell emission is greatly suppressed (or, viewed alternatively, the $h\nu$ = 8.0 – 8.1 keV emission increases approximately linearly with target thickness, while the $h\nu$ = 8.1 to 8.4 keV emission remains low). Thus, resonant self-absorption likely plays a significant role in suppressing the Kβ emission in short-pulse laser experiments.

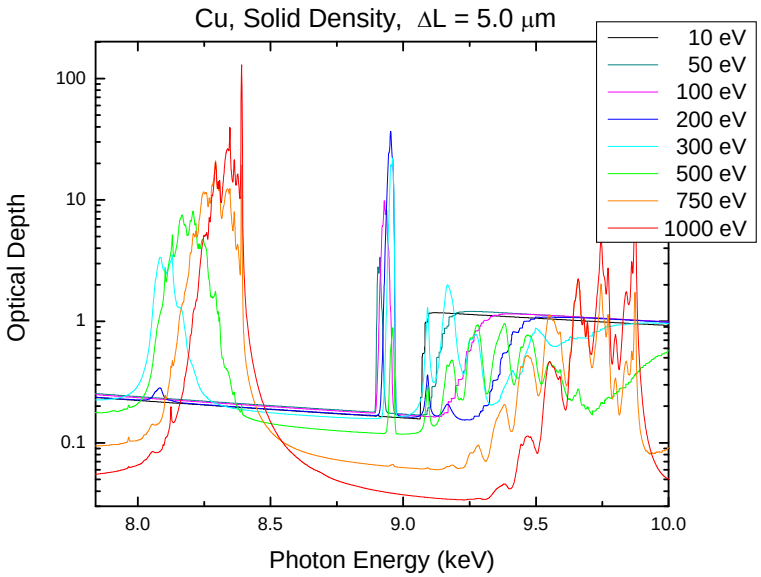

Figure 3.3. Calculated Kα and Kβ optical depths for a 5 μm-thick solid-density Cu target. Optical depths are shown for temperatures ranging from 10 eV to 1 keV.

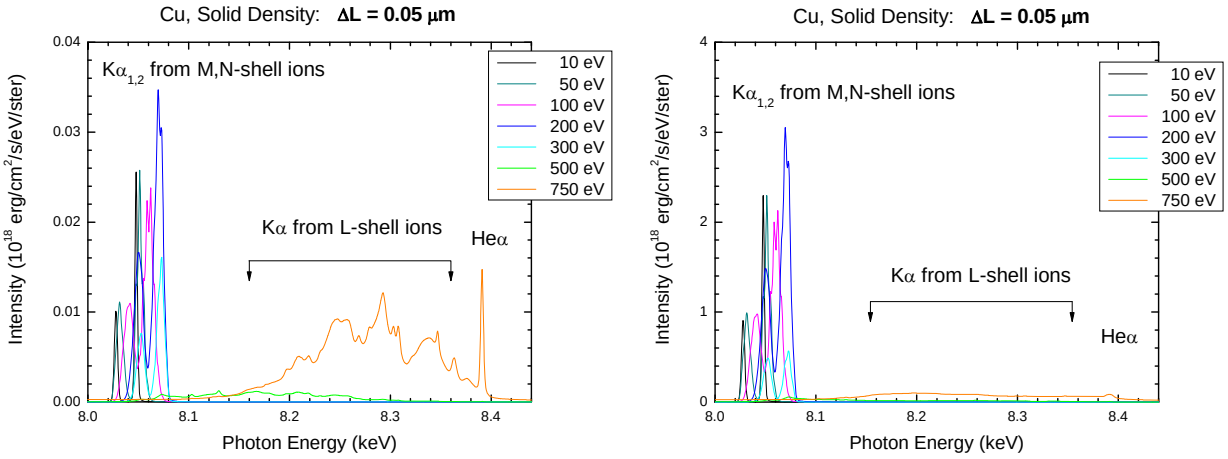

Figure 3.4. Calculated Kα emission spectra for a solid-density Cu target with ΔL = 0.05 μm (left) and ΔL = 5 μm (right). Spectra are shown for temperatures ranging from 10 eV to 750 eV.

We next present results from time-dependent SPECT3D simulations in which streaked spectra were generated for Cu targets. In these simulations, a multi-volume element 2-D cylindrical *r-z* grid was set up using the PlasmaGEN code (see Fig. 3.5). PlasmaGEN is a grid generation code that allows users to specify temperature and density distributions for a multi-volume element grid, and generate files that can be read in by SPECT3D. For this project, PlasmaGEN was upgraded to support specification of hot electron characteristics throughout the grid; in particular, the hot electron temperature, T_{hot}, and either the hot electron fraction, f_{hot}, or density, $N_{e,hot}$. We note that PlasmaGEN also supports generating grids with multiple materials, or layers. Thus, grids can be generated with Kα/Kβ-emitting materials embedded in other materials.

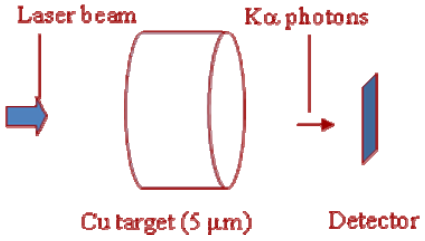

Figure 3.5. Schematic illustration of 2-D cylindrical *r-z* grid set up for Cu target using PlasmaGEN, and location of detector in SPECT3D calculation.

For this series of calculations, all plasma properties (temperature, density, and hot electron characteristics) were spatially uniform. PlasmaGEN was used to generate two grids, the first corresponding to an initial time of $t = 0$, and the second a time of $t = 10$ psec. The thermal temperature at $t = 0$ was $T = 10$ eV. At 10 psec, the thermal temperature was $T = T_{max}$, and it was assumed to vary linearly between these two times, and stay at T_{max} after 10 psec. Four SPECT3D

calculations were run, using T_{max} values of 100, 200, 300, and 400 eV. In all cases, the hot electron density was $N_{e,hot} = 10^{20}$ cm^{-3}, and the hot electron temperature was $T_{hot} = 200$ keV.

Figure 3.6 shows the computed streaked spectra for the four T_{max} cases in the narrow spectral region between $h\nu$ = 7.95 and 8.15 keV. In each case, the streaked spectra were generated using an instrumental resolution of $E/\Delta E$ of 800. For the T_{max} = 100 eV case, the shift in the Kα wavelength between t = 0 and 10 psec is seen to be relatively modest. However, as T_{max} increases up to 400 eV, the shift in wavelength is more pronounced as the higher thermal temperatures lead to higher degrees of ionization in the Cu.

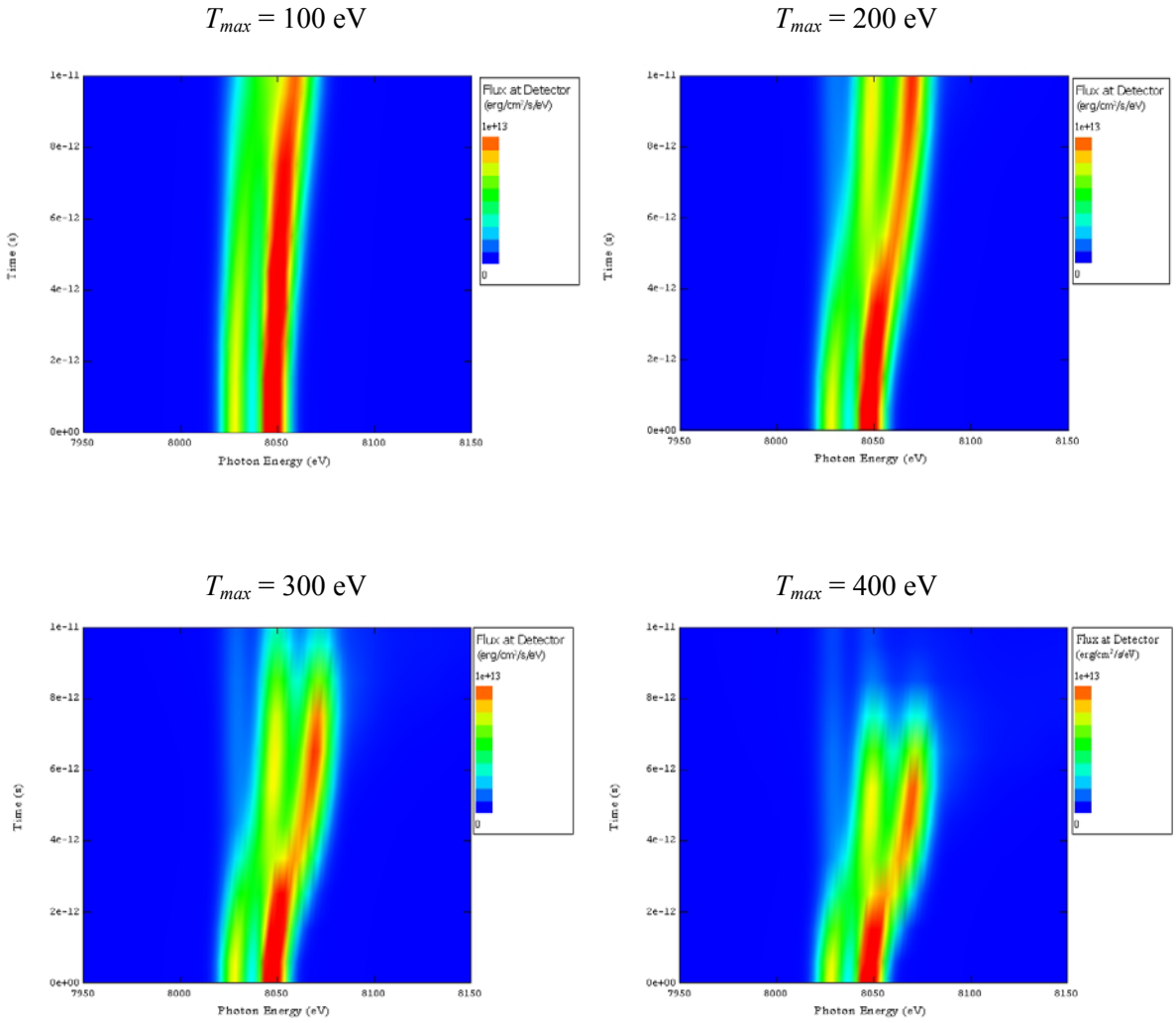

Figure 3.6. Calculated Kα streaked spectra for Cu targets with T_{max} = 100 eV (upper left), 200 eV (upper right), 300 eV (lower left), and 400 eV (lower right).

References

[1] Wang, P., "*Computation and Application of Atomic Data for Inertial Confinement Fusion Plasmas*," Ph.D. Dissertation, Dept of Nuclear Engineering and Engineering Physics, Univ of Wisconsin, Madison, WI (1991).

[2] Fischer, C. F., "*A General Multi-Configuration Hartree-Fock Program*," Comp. Phys. Comm. **14**, 145 (1978).

[3] Fischer, C. F., and Liu, B., "*A Program to Generate Configuration-State Lists*," Comp. Phys. Comm. **64**, 406 (1990).

[4] Fischer, C. F., "*The MCHF Atomic-Structure Package*," Comp. Phys. Comm. **128**, 635 (2000).

[5] Abdallah, J., Clark, R.E.H., and Cowan, R. D., "*Theoretical Atomic Physics Code Development I. CATS: Cowan Atomic Structure Code*," Los Alamos Laboratory Report LA-11436-M, Los Alamos, NM (1988).

[6] Wang, P., MacFarlane, J. J., Moses, G. A., "*Relativistic-Configuration-Interaction Calculations of Kα Satellite Properties for Aluminum Plasmas Created by Intense Proton Beams*," Phys. Rev. E **48**, 3934 (1993).

[7] Wang, P., MacFarlane, J. J., Moses, G. A., "*Thermal Ionization Effects on Inner-Shell Line Emission for Au Targets Heated by Intense Light Ion Beams*," Rev. Sci. Instrum. **63**, 5059 (1992).

[8] Sobelman, I. I., *et al*., "*Excitation of Atoms and Broadening of Spectral Lines*," New York, Springer-Verlag (1981).

[9] McQuarrie, D. A., *Statistical Mechanics*, New York, Harper & Row (1976).

[10] CRC Handbook of Chemistry and Physics, 56th Edition, CRC Press, Cleveland (1975).

[11] Tanis, J. A., Shafroth, S. M., Jacobs, W. W., McAbee, T., and Lapicki, G., Phys. Rev. A **31** (1985).

[12] Holzer, G., Fritsch, M., Deutsch, M., Hartwig, J., and Forster, E., Phys. Rev. A **56**, 4554 (1997).

[13] Chung, H. K., Chen, M. H., Morgan, W. L., Ralchenko, Y., and Lee, R. W., "*FLYCHK: Generalized Population Kinetics and Spectra Model for Rapid Spectroscopic Analysis of All Elements*," High Energy Dens. Phys. **1**, 3 (2005).

[14] Van Regemorter, H., Astrophys. J. **136**, 906 (1962).

[15] Mewe, R., Astron. Astrophys. **20**, 215 (1972).

[16] Burgess, A., and Chidichimo, M. C., Mon. Not. R. Astr. Soc. **203**, 1269 (1983).

[17] Hubbell, J. H., et al., "*A Review, Bibliography, and Tabulation of K, L, and Higher Atomic Shell X-Ray Fluorescence Yields*," J. Phys. Chem. Ref. Data **23**, 339 (1994).

[18] Scofield, J. H., "*Radiative Decay Rates of Vacancies in the K and L Shells*," Phys. Rev. **179**, 9 (1969).

[19] Mihalas D., *Stellar Atmospheres*, New York, W. H. Freeman and Co. (1978).

[20] Karzus, W. J., and Latter, R., "*Electron Radiative Transitions in a Coulomb Field*," Astrophys. J. Sup. Ser. **6**, 167 (1961).

[21] Griem, H. R., "*Semiempirical Formulas for the Electron-Impact Widths and Shifts of Isolated Ion Lines in Plasmas*," Phys. Rev. **165**, 258 (1968).

[22] Hummer, D. G., Mihalas, D., "*The Equation of State for Stellar Envelopes. I. – An Occupation Probability Formalism for the Truncation of Internal Partition Functions*," Astrophys. J. **331**, 794 (1988).

[23] More, R. M., Applied Atomic Collision Physics 2, New York, Academic Press (1982).

[24] Haynes, D. A., private communication (2001).

[25] Iglasius, C. A., DeWitt, H. E., Lebowitz, J. L., MacGowan, D., and Hubbard, W.B., "*Low-Frequency Electric Microfield Distributions in Plasmas*," Phys. Rev. A **31**, 1698 (1985).